CHAPTER IV
# RESULTS AND DISCUSSION

4.1 Photocatalyst Characteracterization Results

### 4.1.1 TG–DTA Results

The TG-DTA curves were used to study the thermal decomposition behavior of the dried synthesized $SrTi_xZr_{1-x}O_3$ and $SrTi_xSi_{1-x}O_3$ gels and obtain their suitable calcination temperatures. Figure 4.1 shows the TG-DTA curves of some selected dried synthesized $SrTiO_3$, $SrZrO_3$, $SrSiO_3$, $SrTi_{0.93}Zr_{0.07}O_3$, and $SrTi_{0.95}Si_{0.05}O_3$ gels. Their corresponding weight losses are shown in Table 4.1. There are three main exothermic regions observed for all the investigated samples, indicating their similar thermal decomposition behavior. The first region lower than 200 °C is attributed to the removal of physisorbed water molecules. The second region approximately between 200 °C and 500 °C is attributed to the burnout of the LAHC surfactant and the residual solvents. The third region, with its position approximately between 500 °C and 650 °C, may be attributed to the crystallization of photocatalyst and the removal of strongly chemisorbed water and organic remnants tightly bonded in the molecular level with Sr, Ti, Zr, and Si metals in the gel network (Khunrattanaphon *et al.*, 2010). The TG results shows the weight losses of all the synthesized $SrTi_xZr_{1-x}O_3$ and $SrTi_xSi_{1-x}O_3$ photocatalysts are finished at the temperature around 650 °C that is sufficient for both the surfactant removal and crystallization process. Consequently, the calcination temperatures in the range of 650 °C to 800 °C were used to study its effect on physicochemical properties and photocatalytic hydrogen production activity of all the synthesized photocatalysts.
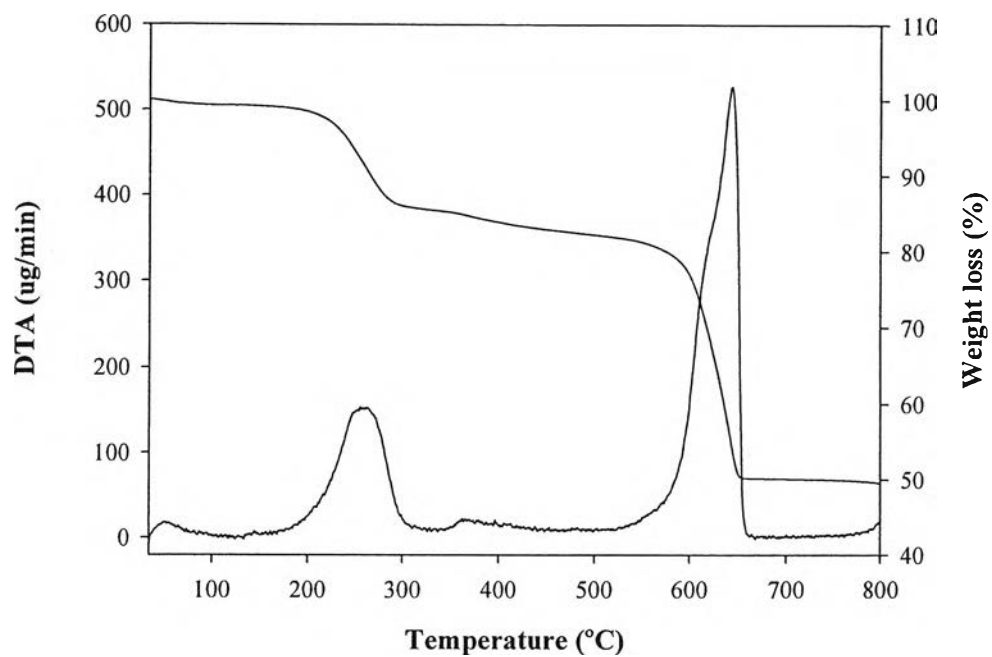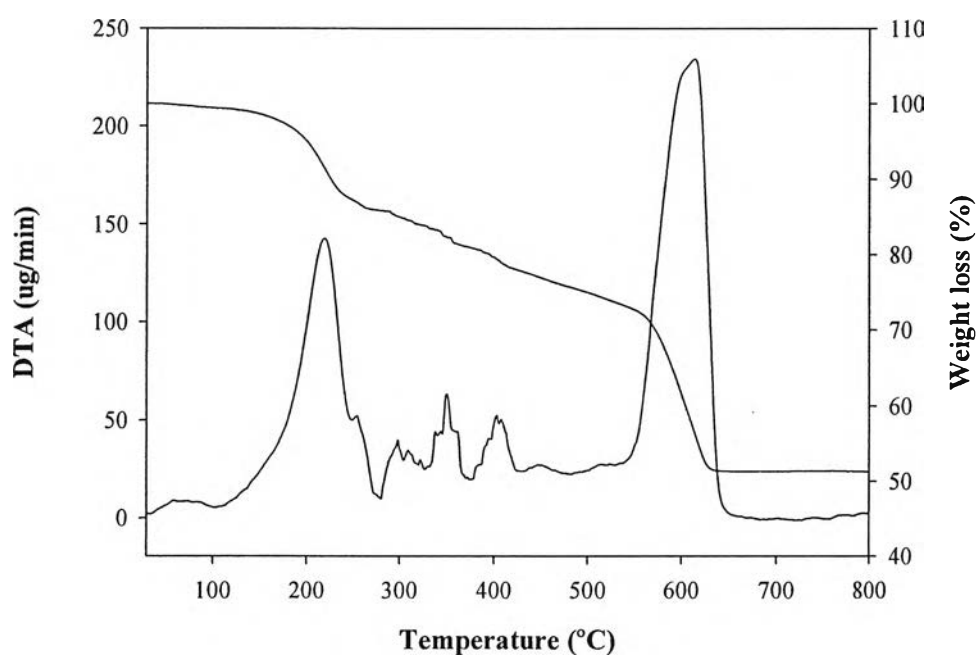
(a)
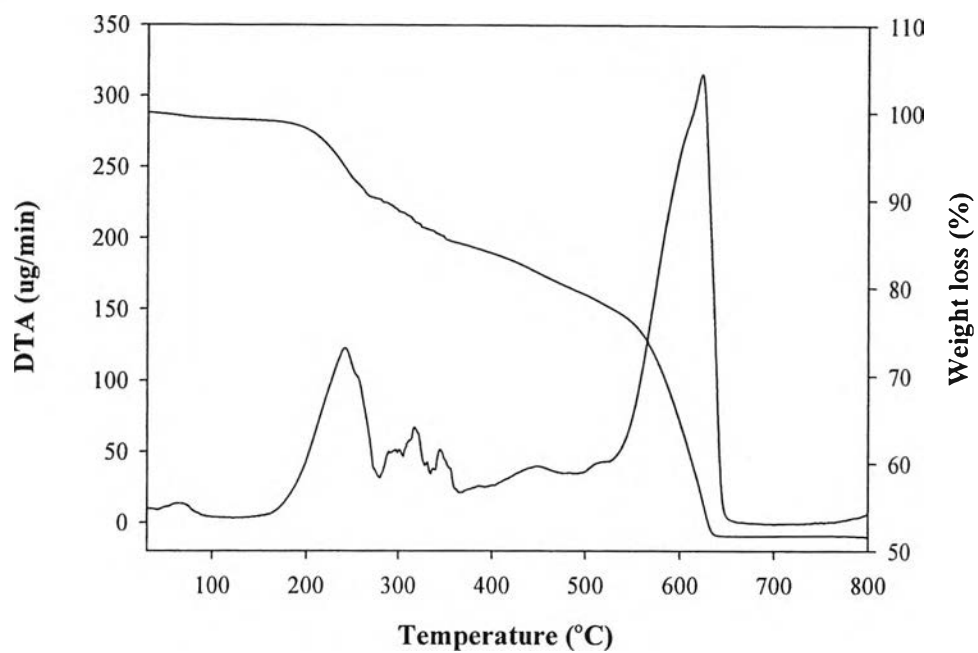
(b)
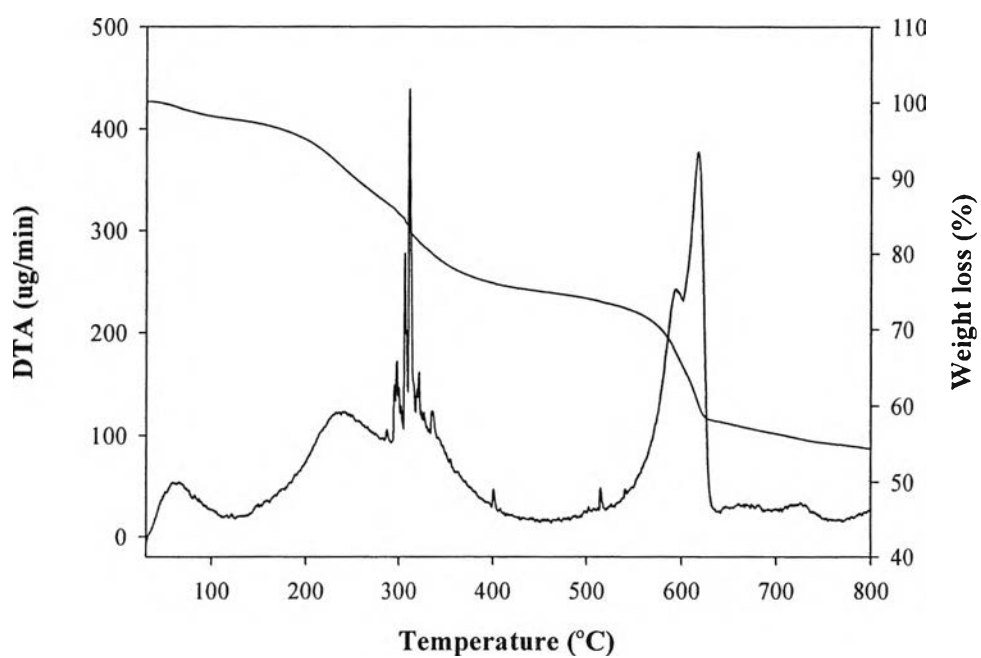
Figure 4.1 TG-DTA curves of the dried synthesized (a) $SrTiO_3$, (b) $SrZrO_3$, (c) $SrSiO_3$, (d) $SrTi_{0.93}Zr_{0.07}O_3$ and (e) $SrTi_{0.95}Si_{0.05}O_3$ photocatalysts.

(c)

(d)

Figure 4.1 (Continued) TG-DTA curves of the dried synthesized (a) SrTiO$_3$,
(b) SrZrO$_3$, (c) SrSiO$_3$, (d) SrTi$_{0.93}$Zr$_{0.07}$O$_3$ and (e) SrTi$_{0.95}$Si$_{0.05}$O$_3$ photocatalysts.
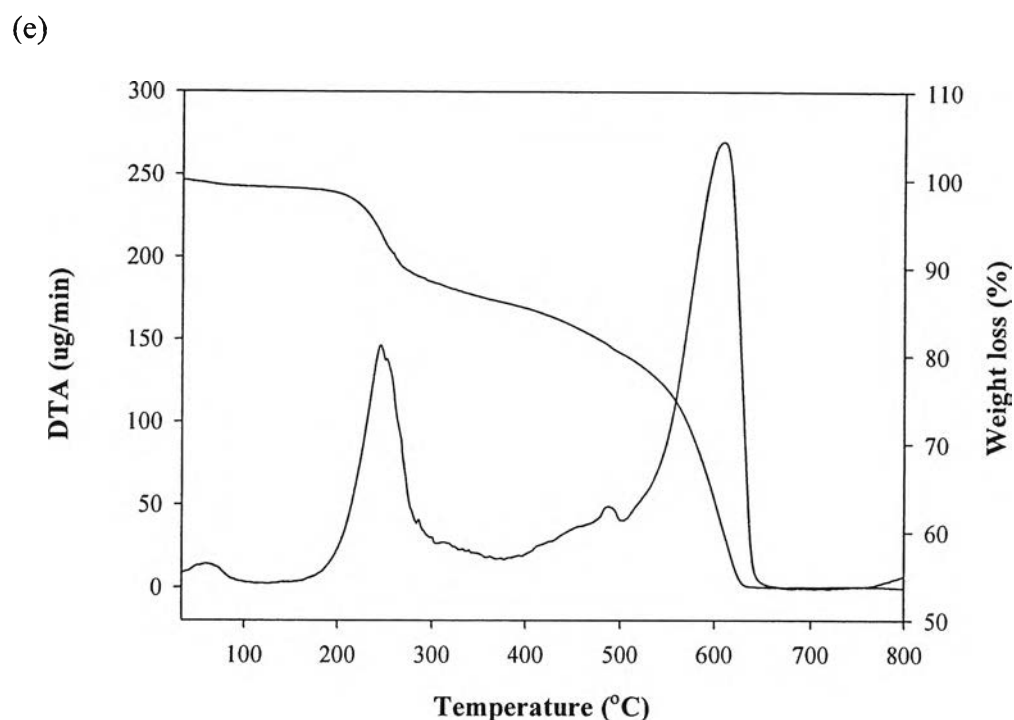
(e)

Figure 4.1 (Continued) TG-DTA curves of the dried synthesized (a) $SrTiO_3$,

(b) $SrZrO_3$, (c) $SrSiO_3$, (d) $SrTi_{0.93}Zr_{0.07}O_3$ and (e) $SrTi_{0.95}Si_{0.05}O_3$ photocatalysts.

Table 4.1 Thermal decomposition behavior results of the dried synthesized $SrTiO_3$, $SrZrO_3$, $SrSiO_3$, $SrTi_{0.93}Zr_{0.07}O_3$ and $SrTi_{0.95}Si_{0.05}O_3$ photocatalysts from TG–DTA analysis

| Photocatalyst	Position of exothermic peak (°C)			Corresponding weight loss (wt.%)			
	1st region	2nd region	3rd region	1st region	2nd region	3rd region	Total
$SrTiO_3$	30–200	200–520	520–650	1.36%	19.90%	26.10%	47.36
$SrZrO_3$	30–180	180–520	520–650	3.40%	23.10%	15.60%	42.10
$SrSiO_3$	30–190	190–510	510–650	1.00%	16.90%	31.70%	49.60
$SrTi_{0.93}Zr_{0.07}O_3$	30–180	190–525	525–650	2.97%	22.78%	21.92%	47.67
$SrTi_{0.95}Si_{0.05}O_3$	30–180	180–500	500–650	0.90%	18.59%	26.24%	45.73

4.1.2 N_2 Adsorption-Desorption Results

In order to verify the mesoporosity of the synthesized photocatalysts, N_2 adsorption-desorption analysis is an important technique normally used. The shape of the isotherms exhibits the characteristic behavior of the structure of powder, which is composed of an assembly of particles with uniform pore opening. The N_2 adsorption-desorption isotherms of the $SrTiO_3$, $SrTi_{0.93}Zr_{0.07}O_3$, $SrTi_{0.95}Si_{0.05}O_3$, 0.25 wt.% Cu-loaded $SrTi_{0.93}Zr_{0.07}O_3$, and 0.75 wt.% Cu-loaded $SrTi_{0.95}Si_{0.05}O_3$ calcined at 700 °C are exemplified in Figure 4.2. All of the samples exhibit typical IUPAC type IV pattern with a hysteresis loop, which is the characteristic of a mesoporous-assembled material (mesoporous size between 2 nm to 50 nm) according to the classification of IUPAC (Rouquerol et al., 1999). A sharp increase in the adsorption curves at a high relative pressure implies a capillary condensation of N_2 molecule inside the mesopores, implying the well-uniform mesopores and narrow pore size distribution since the P/P_0 position of the inflection point is directly related to the pore dimension (Sreethawong *et al.*, 2005). The insets of Figure 4.2 show pore size distributions calculated from the desorption branch of the isotherms by the DH method. It can be clearly seen that all of samples possessed very narrow pore size distribution in the mesopore region, identifying a good quality of the samples. This also verifies a well-controlled pore size of the photocatalysts synthesized by the sol-gel process with the aid of a structure-directing surfactant in this present work.

The textural properties obtained from N_2 adsorption-desorption isotherms, i.e. specific surface area, mean mesopore diameter, and total pore volume, of all investigated photocatalysts, are summarized in Table 4.2. The specific surface area increases with increasing Zr molar ratio in the $SrTi_xZr_{1-x}O_3$ photocatalysts as well as with increasing Si molar ratio in the $SrTi_xSi_{1-x}O_3$ photocatalysts when compared with $SrTiO_3$. In case of increasing calcination temperature from 650 °C to 800 °C for the $SrTi_{0.95}Si_{0.05}O_3$ photocatalyst, it can be seen from Table 4.2 that the specific surface area tends to decrease with increasing calcination temperature because of the pore collapse due to both the destruction of walls separating the mesopores upon the crystallization and the grain growth of the photocatalyst crystallites. This consequently led to an increase in the mean mesopore diameter with a simultaneous decrease in the total pore volume.

The textural properties of the synthesized Cu-loaded $SrTi_{0.93}Zr_{0.07}O_3$ and Cu-loaded $SrTi_{0.95}Si_{0.05}O_3$ photocatalysts calcined at 700 °C with various Cu loadings are shown in Table 4.3. The results show a slightly positive effect of Cu loading on the specific surface area as compared to the unloaded $SrTi_{0.93}Zr_{0.07}O_3$ and $SrTi_{0.95}Si_{0.05}O_3$ photocatalysts, while the mean mesopore diameter and total pore volume were only slightly varied with Cu loadings, indicating that the loaded metal particles did not block the mesopores (Onsuratoom *et al.*, 2011).
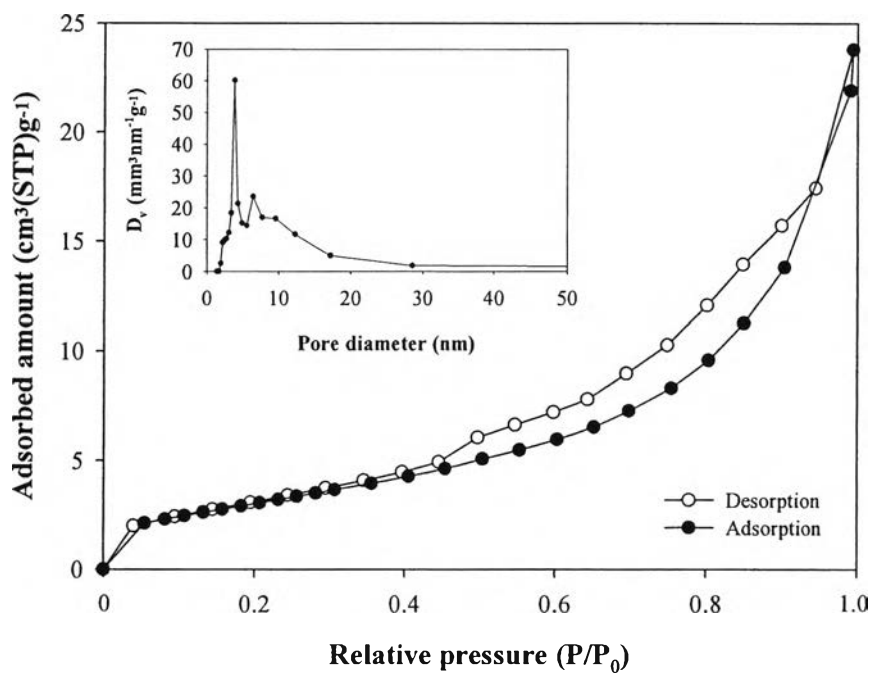
(a)
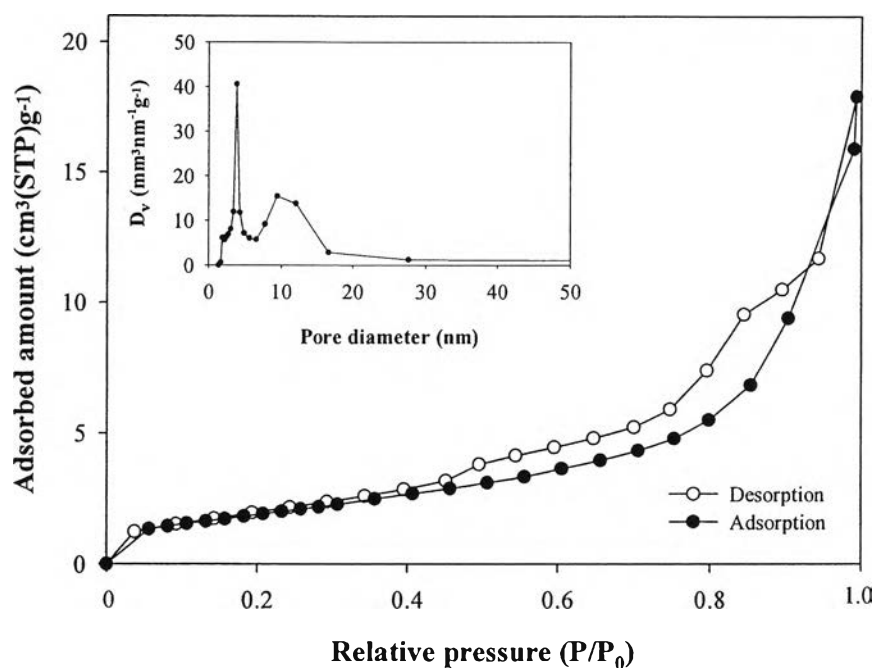
Figure 4.2 N_2 adsorption-desorption isotherms and pore size distributions (inset) of the synthesized (a) $SrTiO_3$, (b) $SrTi_{0.93}Zr_{0.07}O_3$, (c) $SrTi_{0.95}Si_{0.05}O_3$, (d) 0.25 wt.% Cu loaded $SrTi_{0.93}Zr_{0.07}O_3$, and (e) 0.75 wt.% Cu loaded $SrTi_{0.95}Si_{0.05}O_3$ photocatalysts calcined at 700 °C for 4 h.

(b)
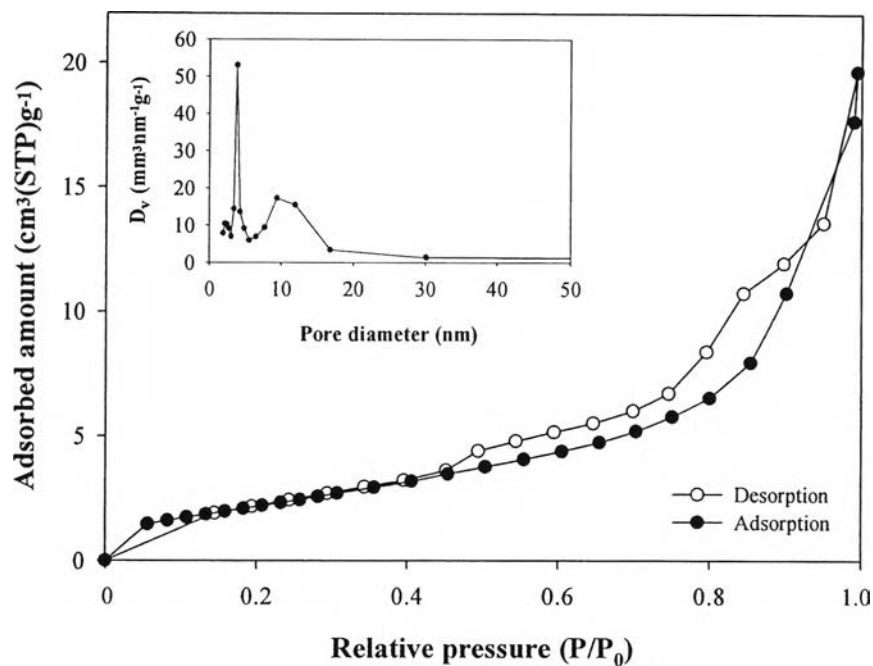
(c)

Figure 4.2 **(Continued)** N$_2$ adsorption-desorption isotherms and pore size distributions (inset) of the synthesized (a) SrTiO$_3$, (b) SrTi$_{0.93}$Zr$_{0.07}$O$_3$, (c) SrTi$_{0.95}$Si$_{0.05}$O$_3$, (d) 0.25 wt.% Cu loaded SrTi$_{0.93}$Zr$_{0.07}$O$_3$, and (e) 0.75 wt.% Cu loaded SrTi$_{0.95}$Si$_{0.05}$O$_3$ photocatalysts calcined at 700 °C for 4 h.
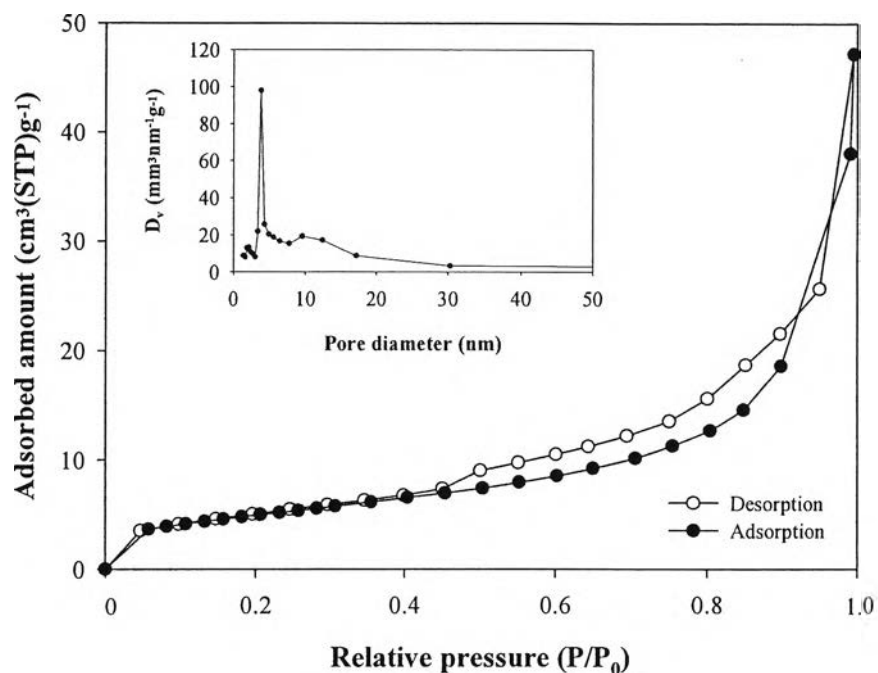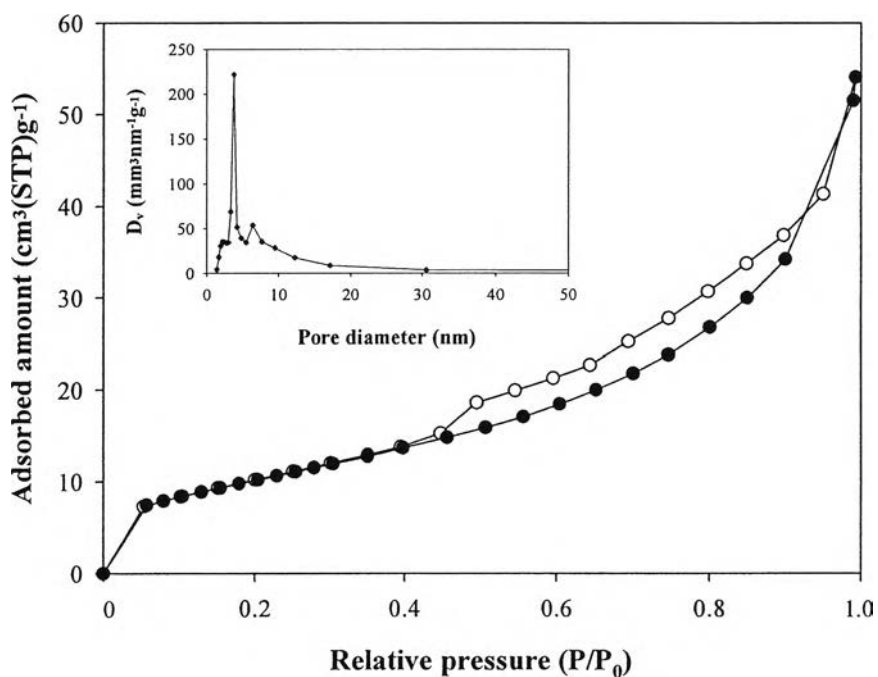
(d)

(e)

Figure 4.2 (Continued) N_2 adsorption-desorption isotherms and pore size distributions (inset) of the synthesized (a) $SrTiO_3$, (b) $SrTi_{0.93}Zr_{0.07}O_3$, (c) $SrTi_{0.95}Si_{0.05}O_3$, (d) 0.25 wt.% Cu loaded $SrTi_{0.93}Zr_{0.07}O_3$, and (e) 0.75 wt.% Cu loaded $SrTi_{0.95}Si_{0.05}O_3$ photocatalysts calcined at 700 °C for 4 h.

Table 4.2 N_2 adsorption-desorption results of the synthesized mesoporous-assembled $SrTi_xZr_{1-x}O_3$ and $SrTi_xSi_{1-x}O_3$ photocatalysts

Photocatalyst	Calcination temperature (°C)	Specific surface area $(m^2 \cdot g^{-1})$	Mean mesopore diameter (nm)	Total pore volume $(cm^3 \cdot g^{-1})$
$SrTiO_3$	700	7.20	3.80	0.028
$SrTi_{0.97}Zr_{0.03}O_3$		8.09	3.77	0.030
$SrTi_{0.95}Zr_{0.05}O_3$		8.24	3.78	0.032
$SrTi_{0.93}Zr_{0.07}O_3$	700	8.66	3.82	0.031
$SrTi_{0.91}Zr_{0.09}O_3$		12.36	3.78	0.062
$SrTi_{0.89}Zr_{0.11}O_3$		12.53	3.82	0.065
$SrTi_{0.97}Si_{0.03}O_3$		8.44	3.79	0.036
$SrTi_{0.95}Si_{0.05}O_3$		11.54	3.80	0.038
$SrTi_{0.93}Si_{0.07}O_3$	700	16.87	3.82	0.044
$SrTi_{0.91}Si_{0.09}O_3$		17.56	3.81	0.060
$SrTi_{0.89}Si_{0.11}O_3$		18.28	3.83	0.070
$SrTi_{0.95}Si_{0.05}O_3$	650	14.61	3.73	0.040
	700	11.54	3.82	0.038
	800	7.88	4.26	0.032

Table 4.3 N_2 adsorption-desorption results of the synthesized Cu-loaded mesoporous-assembled $SrTi_{0.93}Zr_{0.07}O_3$ and $SrTi_{0.95}Si_{0.05}O_3$ photocatalysts

Photocatalyst	Cu loading (wt.%)	Specific surface area (m^2g^{-1})	Mean mesopore diameter (nm)	Total pore volume $(cm^3 \cdot g^{-1})$
$SrTi_{0.93}Zr_{0.07}O_3$	0	8.66	3.82	0.031
	0.25	18.99	3.83	0.072
	0.50	16.94	3.83	0.048
	0.75	18.24	3.83	0.058
	1.0	17.98	3.83	0.060
	1.25	18.66	3.83	0.062
$SrTi_{0.95}Si_{0.05}O_3$	0	11.54	3.80	0.038
	0.25	37.43	3.81	0.082
	0.50	36.67	3.79	0.082
	0.75	39.05	3.79	0.083
	1.00	37.43	3.82	0.091
	1.25	38.86	3.81	0.080

4.1.3 XRD Results

The X-ray diffraction was used to identify the crystallinity and crystallite size of the photocatalysts. The XRD patterns of the synthesized mesoporous-assembled $SrTi_xZr_{1-x}O_3$ and $SrTi_xSi_{1-x}O_3$ photocatalysts calcined at 700 °C are shown in Figure 4.3. The dominant peaks at 2θ of about 32.4, 39.9, 46.4, 57.8, 67.8, and 77.2°, which represent the indices of (110), (111), (200), (211), (220), and (310) planes, respectively, could be indexed to the $SrTiO_3$ with a cubic perovskite structure (JCPDS card no. 35-0734) (Smith, 1996). However, in case of x = 0 for $SrTi_xSi_{1-x}O_3$ photocatalyst calcined at 700 °C, the $SrSiO_3$ phase could not be obtained as expected, whereas the main crystalline phase of Sr_2SiO_4 was observed (JCPDS card no. 39-1256) (Hsu, et al., 2009). From Figure 4.3(a), the diffraction peaks of $SrTiO_3$, as clearly observed for the (110) plane at 2θ of 32.4°, slightly

shifted to a lower diffraction angle with increasing the Zr molar ratio, which could confirm the existence of zirconium in the form of solid solution in the synthesized $SrTi_xZr_{1-x}O_3$ photocatalysts (Khunrattanaphon *et al.*, 2011). On the other hand, an increase in the Si molar ratio in the $SrTi_xSi_{1-x}O_3$ photocatalysts did not change diffraction angle of the diffraction peaks of $SrTiO_3$, as shown in Figure 4.3(b). The diffraction peak at 25.2°, which represents the index of $SrCO_3$ (111) plane, showed the present of $SrCO_3$ impurity, which unavoidably coexists in the resulting $SrTi_xZr_{1-x}O_3$ and $SrTi_xSi_{1-x}O_3$ photocatalysts during the synthesis and calcination processes (Khunrattanaphon *et al.*, 2011). In case of the effect calcination temperature as shown in Figure 4.4, it was found that the purity and crystallinity of the synthesized $SrTi_{0.95}Si_{0.05}O_3$ photocatalyst increased with increasing calcination temperature (Puangpetch *et al.*, 2008). However, the presence of the Cu phase in the XRD patterns could not be observed, which is probably due to its low content with a high dispersion degree on the surface of $SrTi_{0.93}Zr_{0.07}O_3$ and $SrTi_{0.95}Si_{0.05}O_3$ photocatalysts calcined at 700 °C (Onsuratoom *et al.*, 2011), as shown in Figure 4.5.

The crystallite size of all the synthesized photocatalysts were calculated from the line broadening of the XRD peak of each crystalline phase according to the Scherrer equation (Cullity, 1987) (Eq. 4.1):

$$L = \frac{k\lambda}{\beta \cos(\theta)} \qquad (4.1)$$

where L is the crystallite size, k is the Scherrer constant usually taken as 0.89, λ is the wavelength of the X-ray radiation (0.15418 nm for Cu Kα), β is the full width at half maximum (FWHM) of the diffraction peak measured at 2θ, and θ is the diffraction angle. The crystallite sizes of the synthesized $SrTi_xZr_{1-x}O_3$ and $SrTi_xSi_{1-x}O_3$ photocatalysts calculated from the $SrTiO_3$ (110) line broadening are about 26 nm to 28 nm, as shown in Table 4.4. The results clearly reveal that the crystallite sizes tend to slightly decrease with increasing Zr or Si molar ratio. In contrast, an increase in the calcination temperature of the synthesized $SrTi_{0.95}Si_{0.05}O_3$ photocatalyst resulted in slightly larger crystallite sizes. From Table 4.5, the crystallite size of the Cu-loaded $SrTi_{0.93}Zr_{0.07}O_3$ and Cu-loaded $SrTi_{0.95}Si_{10.05}O_3$ photocatalysts slightly differed from the unloaded $SrTi_{0.93}Zr_{0.07}O_3$ and $SrTi_{0.95}Si_{10.05}O_3$ photocatalysts. Therefore, the results point out that the Cu loading with such relatively low contents

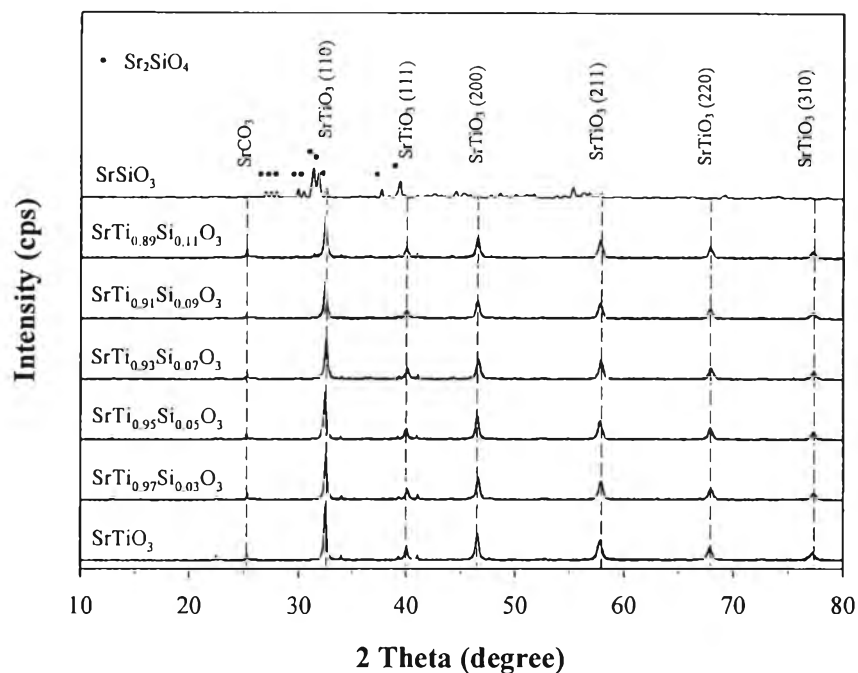insignificantly affected the crystallite sizes of the $SrTi_{0.93}Zr_{0.07}O_3$ and $SrTi_{0.95}Si_{10.05}O_3$ photocatalysts.

(a)
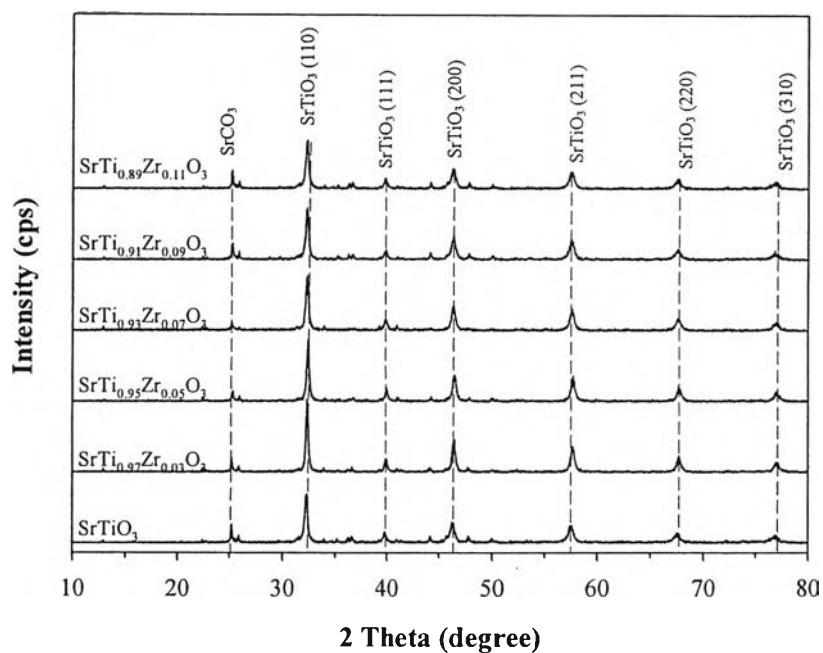
Figure 4.3 XRD patterns of the synthesized (a) $SrTi_xZr_{1-x}O_3$ and (b) $SrTi_xSi_{1-x}O_3$ photocatalysts calcined at 700 °C for 4 h.
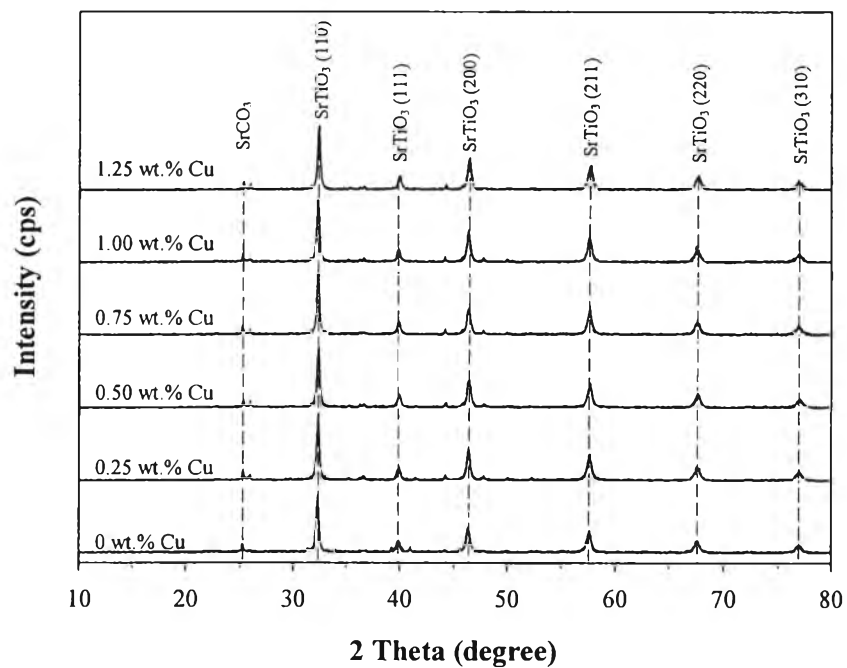
(b)

Figure 4.3 (Continued) XRD patterns of the synthesized (a) $SrTi_xZr_{1-x}O_3$ and (b) $SrTi_xSi_{1-x}O_3$ photocatalysts calcined at 700 °C for 4 h.
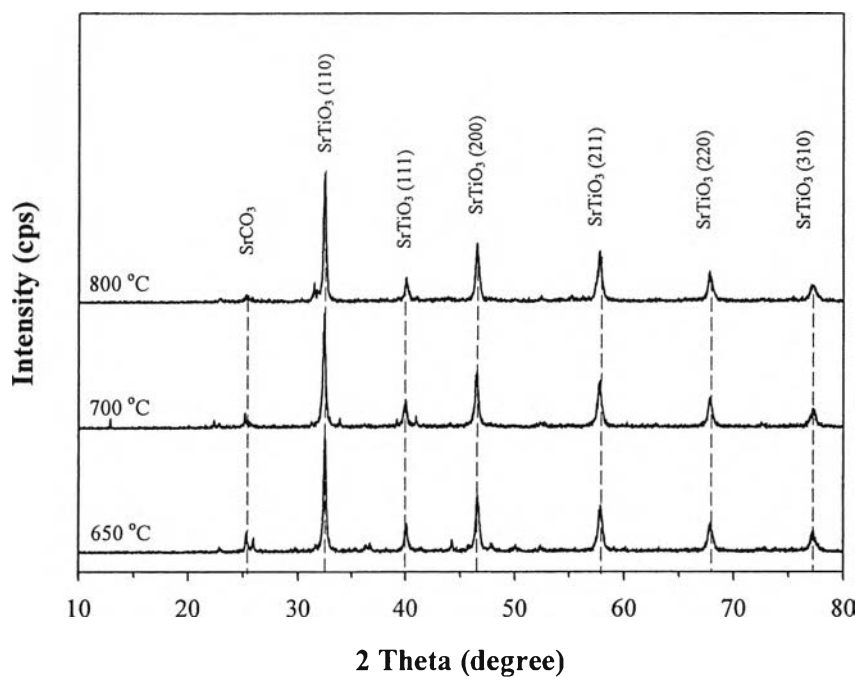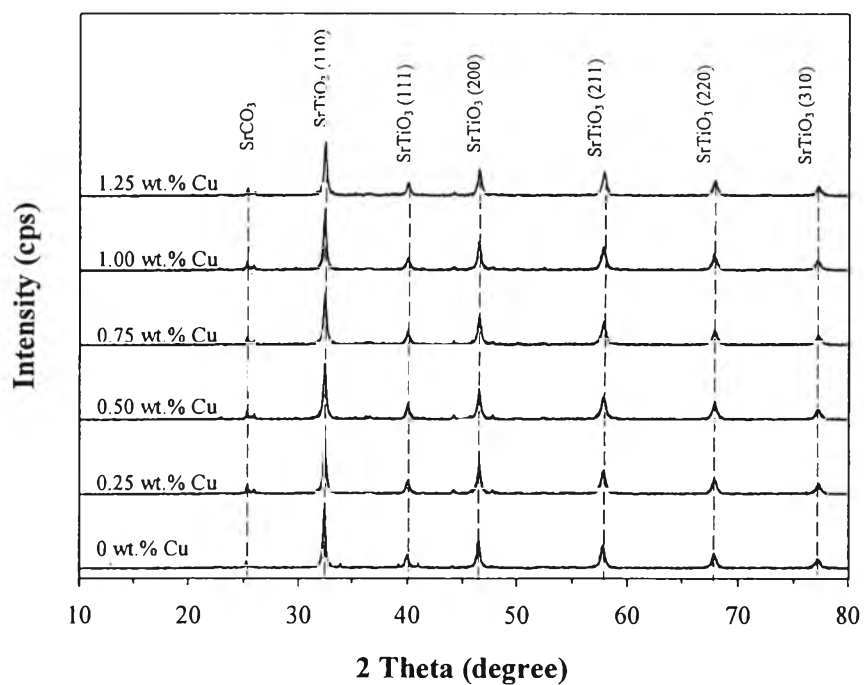

Figure 4.4 XRD patterns of the synthesized $SrTi_{0.95}Si_{0.05}O_3$ photocatalyst calcined at various temperatures for 4 h.

(a)

(b)

Figure 4.5 XRD patterns of the Cu-loaded synthesized (a) $SrTi_{0.93}Zr_{0.07}O_3$ and (b) $SrTi_{0.95}Si_{0.05}O_3$ photocatalysts with various Cu loadings calcined at 700 °C for 4 h.

Table 4.4 Summary of XRD analysis of the synthesized mesoporous-assembled $SrTi_{0.93}Zr_{0.07}O_3$ and $SrTi_{0.95}Si_{0.05}O_3$ photocatalysts

Photocatalyst	Calcination temperature (°C)	Phase from XRD pattern	$SrTiO_3$ (110) crystallite size (nm)
$SrTiO_3$	700	Cubic	27.85
$SrTi_{0.97}Zr_{0.03}O_3$			27.75
$SrTi_{0.95}Zr_{0.05}O_3$			27.48
$SrTi_{0.93}Zr_{0.07}O_3$	700	Cubic	25.74
$SrTi_{0.91}Zr_{0.09}O_3$			25.34
$SrTi_{0.89}Zr_{0.11}O_3$			25.18
$SrTi_{0.97}Si_{0.03}O_3$			26.85
$SrTi_{0.95}Si_{0.05}O_3$			26.67
$SrTi_{0.93}Si_{0.07}O_3$	700	Cubic	25.44
$SrTi_{0.91}Si_{0.09}O_3$			25.27
$SrTi_{0.89}Si_{0.11}O_3$			25.19
$SrTi_{0.95}Si_{0.05}O_3$	650	Cubic	26.42
	700		26.67
	800		27.03

Table 4.5 Summary of XRD analysis of the synthesized Cu-loaded mesoporous-assembled $SrTi_{0.93}Zr_{0.07}O_3$ and $SrTi_{0.95}Si_{0.05}O_3$ photocatalysts

| Photocatalyst	Cu loading (wt.%)	Phase from XRD pattern	$SrTiO_3$ (110) crystallite size (nm)
$SrTi_{0.93}Zr_{0.07}O_3$	0	Cubic	25.74
	0.25		25.03
	0.50		25.19
	0.75		25.27
	1.00		25.42
	1.25		25.43
$SrTi_{0.95}Si_{0.05}O_3$	0	Cubic	26.67
	0.25		25.91
	0.50		24.59
	0.75		24.81
	1.00		25.19
	1.25		25.43

4.1.4 UV-Visible Spectroscopy Results

The light absorption ability of all the synthesized photocatalysts was examined by using UV-visible spectroscopy. The UV-visible spectra of the synthesized mesoporous-assembled $SrTiO_3$, $SrTi_xZr_{1-x}O_3$, and $SrTi_xSi_{1-x}O_3$ photocatalysts calcined at 700 °C are exemplified in Figures 4.6 and 4.7. It can be clearly observed that the absorption band of the synthesized $SrTi_xZr_{1-x}O_3$ and $SrTi_xSi_{1-x}O_3$ photocatalysts was mainly located in the UV region with wavelength of 200 nm to 400 nm. The band gap energy (E_g, eV) was determined by extrapolating the absorption onset of the rising part to x-axis (λ_g, nm) of the plots and calculated by Eq. (4.2):

$$E_g = 1240 / \lambda_g \tag{4.2}$$

where λ_g is the wavelength (nm) of the exciting light. The results of absorption onset wavelength and corresponding band gap energy of all the photocatalysts are summarized in Table 4.6. The absorption onset wavelength of synthesized $SrTi_xZr_{1-x}O_3$ and $SrTi_xSi_{1-x}O_3$ photocatalysts slightly shifted to shorter value (higher value of band gap energy) with increasing Zr or Si molar ratio, e.g. from 395 nm ($E_g = 3.14$ eV) of the $SrTiO_3$ to 391 nm ($E_g = 3.17$ eV) of the $SrTi_{0.89}Zr_{0.11}O_3$ or to 390 nm ($E_g = 3.18$eV) of the $SrTi_{0.89}Si_{0.11}O_3$ photocatalysts. In case of increasing calcination temperature from 650 to 800 °C of the $SrTi_{0.95}Si_{0.05}O_3$ photocatalyst as shown in Figure 4.8, the gradual shift of the absorption onset edge toward a longer wavelength could be observed. As also included in Table 4.6, the band gap energy of the $SrTi_{0.95}Si_{0.05}O_3$ photocatalyst slightly decreased from 3.18 eV ($\lambda_g = 390$ nm) at the calcination temperature of 650 °C to 3.15 eV ($\lambda_g = 394$ nm) at the calcination temperature of 800 °C. The comparative results of UV-visible spectra of the mesoporous-assembled $SrTi_{0.93}Zr_{0.07}O_3$ and $SrTi_{0.95}Si_{0.05}O_3$ photocatalysts calcined at 700 °C without and with 0.25 wt.% and 0.75 wt.% Cu loadings, respectively, are exemplified in Figure 4.9. It can be observed that their UV light absorption ability is in the following order: 0.75 wt.% Cu-loaded $SrTi_{0.95}Si_{0.05}O_3$ > 0.25 wt.% Cu-loaded $SrTi_{0.93}Zr_{0.07}O_3$ > $SrTi_{0.93}Zr_{0.07}O_3$ > $SrTi_{0.95}Si_{0.05}O_3$ photocatalysts. The difference is their light absorption ability significantly affected their photocatalytic activity in this work, as shown later.
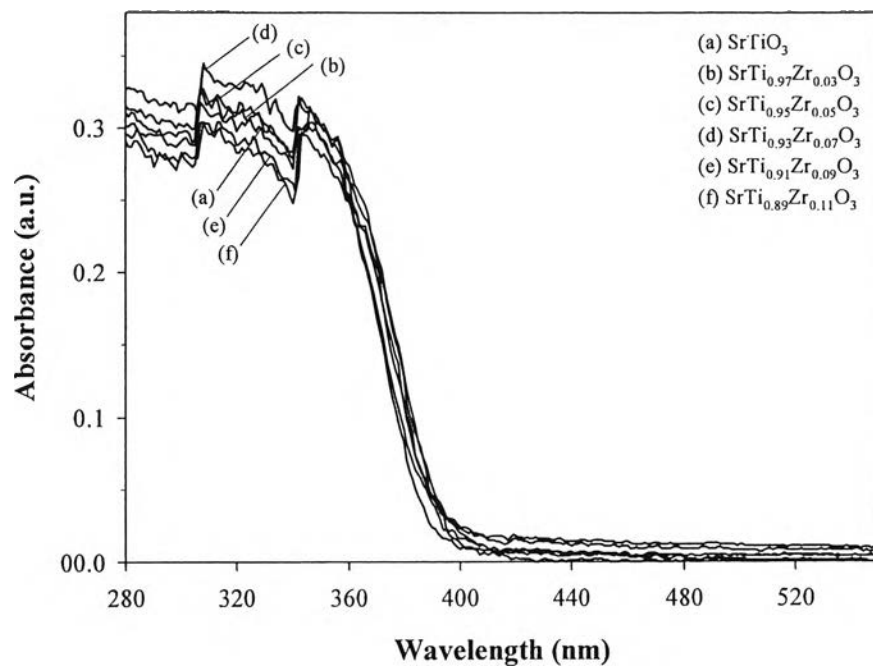
Figure 4.6 UV-visible spectra of the synthesized mesoporous-assembled photocatalysts calcined at 700 °C for 4 h: (a) $SrTiO_3$ and (b)-(f) $SrTi_xZr_{1-x}O_3$.
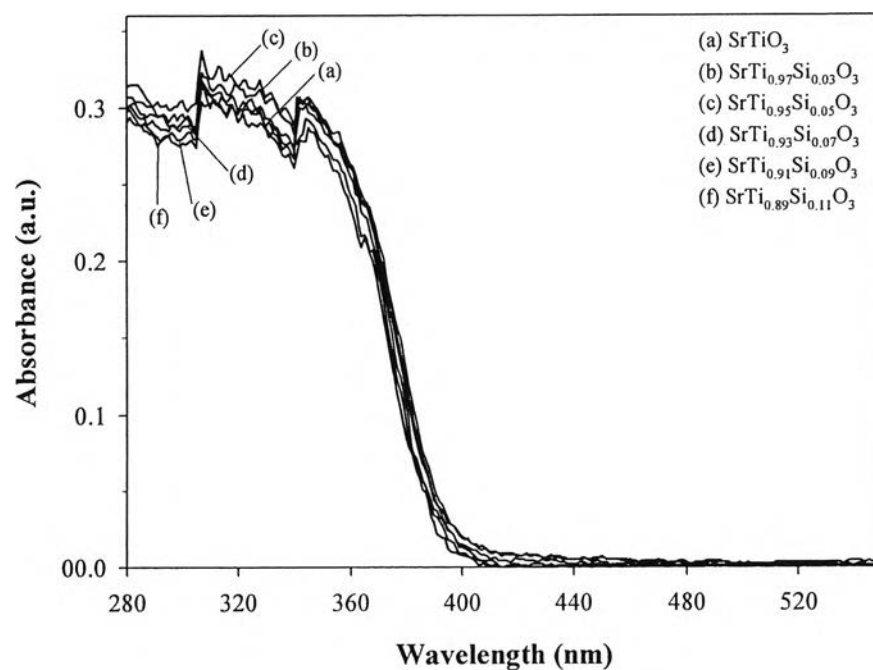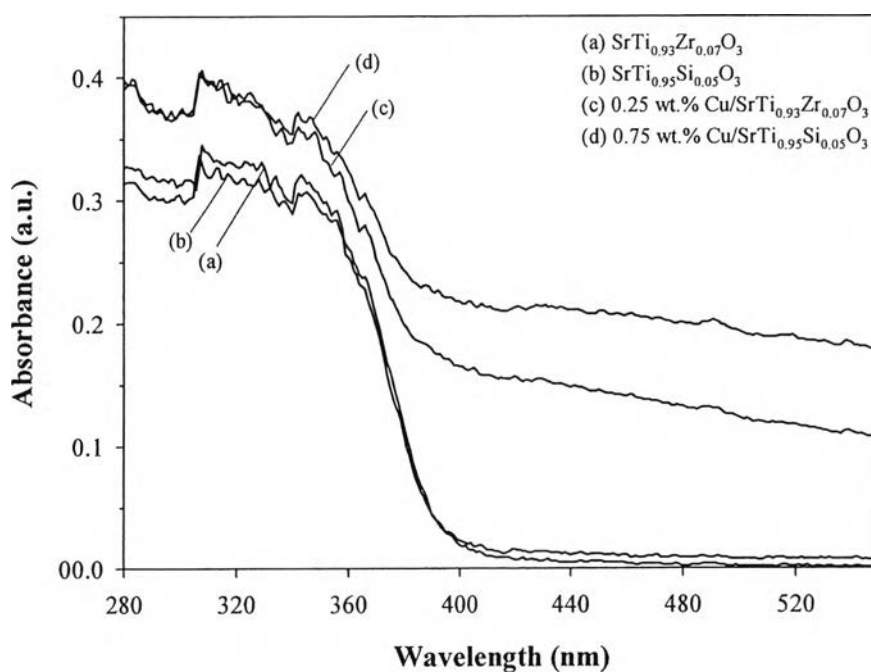

Figure 4.7 UV-visible spectra of the synthesized mesoporous-assembled photocatalysts calcined at 700 °C for 4 h: (a) $SrTiO_3$ and (b)-(f) $SrTi_xSi_{1-x}O_3$.
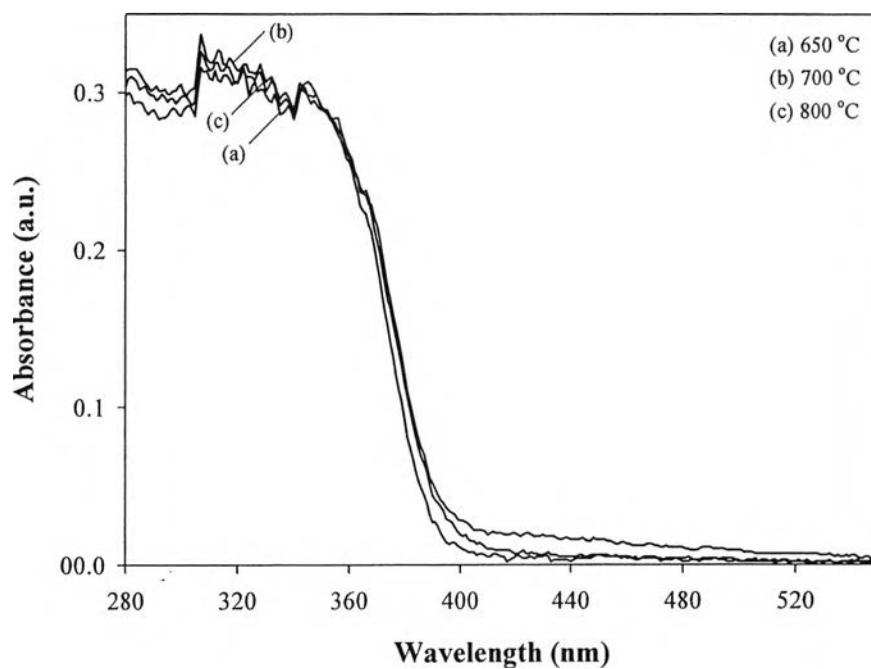
Figure 4.8 UV-visible spectra of the synthesized mesoporous-assembled SrTi$_{0.95}$Si$_{0.05}$O$_3$ photocatalyst calcined at various temperatures for 4 h.
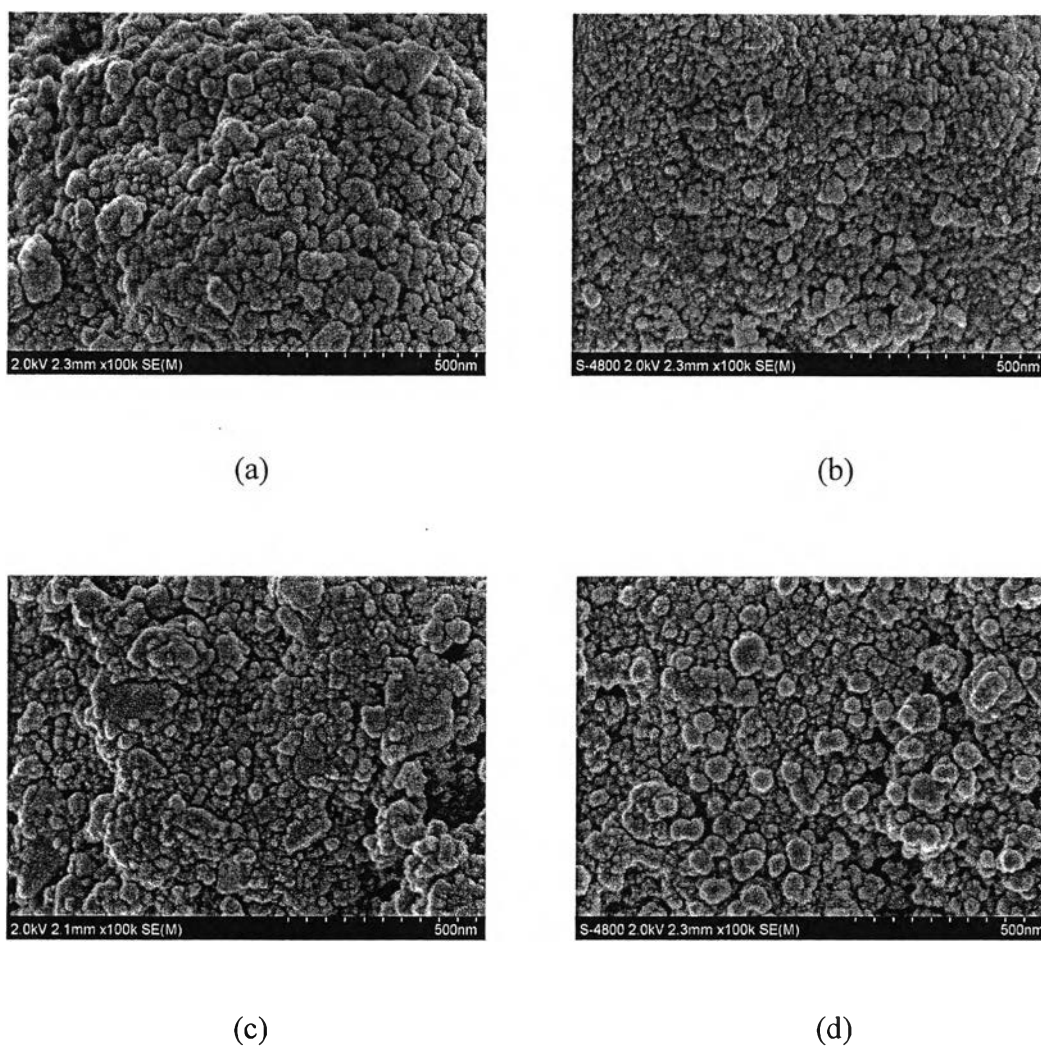

Figure 4.9 UV-visible spectra of the synthesized mesoporous-assembled photocatalysts calcined at 700 °C for 4 h: (a) SrTi$_{0.93}$Zr$_{0.07}$O$_3$, (b) SrTi$_{0.95}$Si$_{0.05}$O$_3$, (c) 1.25 wt.% Cu-loaded SrTi$_{0.93}$Zr$_{0.07}$O$_3$, and (d) 0.75 wt.% Cu-loaded SrTi$_{0.95}$Si$_{0.05}$O$_3$.

Table 4.6 Absorption onset wavelength and band gap energy results of the synthesized mesoporous-assembled $SrTi_xZr_{1-x}O_3$ and $SrTi_xSi_{1-x}O_3$ photocatalysts without and with Cu loadings and calcined at various temperatures

| Photocatalyst	Calcination temperature (°C)	Absorption onset wavelength, λ_g (nm)	Band gap energy (eV)
$SrTiO_3$	700	395	3.14
$SrTi_{0.97}Zr_{0.03}O_3$	700	394	3.15
$SrTi_{0.95}Zr_{0.05}O_3$		394	3.15
$SrTi_{0.93}Zr_{0.07}O_3$		392	3.16
$SrTi_{0.91}Zr_{0.09}O_3$		391	3.17
$SrTi_{0.89}Zr_{0.11}O_3$		391	3.17
$SrTi_{0.97}Si_{0.03}O_3$	700	395	3.14
$SrTi_{0.95}Si_{0.05}O_3$		392	3.16
$SrTi_{0.93}Si_{0.07}O_3$		391	3.17
$SrTi_{0.91}Si_{0.09}O_3$		391	3.17
$SrTi_{0.89}Si_{0.11}O_3$		390	3.18
$SrTi_{0.95}Si_{0.05}O_3$	650	390	3.18
	700	392	3.16
	800	394	3.15
0.25 wt.% Cu-loaded $SrTi_{0.93}Zr_{0.07}O_3$	700	387	3.20
0.75 wt.% Cu-loaded $SrTi_{0.95}Si_{0.05}O_3$	700	389	3.19

4.1.5 SEM-EDX Results

The external morphology of the photocatalysts was observed by the SEM analysis. Figure 4.10 comparatively represents the SEM images of the mesoporous-assembled $SrTi_{0.93}Zr_{0.07}O_3$ and $SrTi_{0.95}Si_{0.05}O_3$ photocatalysts calcined at 700 °C without and with 0.25 wt.% and 0.75 wt.% Cu loadings, respectively. All the SEM images clearly reveal the presence of agglomerated clusters formed by an aggregation of several uniform-sized photocatalyst nanoparticles. Hence, the nanoparticle aggregation plausibly led to the formation of mesoporous-assembled structure in the synthesized photocatalysts. The elemental distributions on the 0.25 wt.% Cu-loaded $SrTi_{0.93}Zr_{0.07}O_3$, and 0.75 wt.% Cu-loaded $SrTi_{0.95}Si_{0.05}O_3$ photocatalysts calcined at 700 °C were also examined by using the EDX analysis, as shown in Figures 4.11 and 4.12, respectively. The existence of dots in the elemental mappings of all investigated species (Sr, Ti, Zr, Si, O, and Cu) indicates that all the elements in the Cu-loaded $SrTi_{0.93}Zr_{0.07}O_3$, and Cu-loaded $SrTi_{0.95}Si_{0.05}O_3$ photocatalysts were well dispersed throughout the bulk photocatalysts. These results confirm the high dispersion state of the loaded Cu particles on the synthesized photocatalysts prepared by the PCD method.

(a)

(b)

(c)

(d)

Figure 4.10 SEM images of the synthesized mesoporous-assembled photocatalysts calcined at 700 °C for 4 h: (a) $SrTi_{0.93}Zr_{0.07}O_3$, (b) 0.25 wt.% Cu-loaded $SrTi_{0.93}Zr_{0.07}O_3$, (c) $SrTi_{0.95}Si_{0.05}O_3$ and (d) 0.75 wt.% Cu-loaded $SrTi_{0.95}Si_{0.05}O_3$.

Electron Image 1

O Ka1

Sr Ka1

Ti Ka1

Zr La1

Cu Ka1
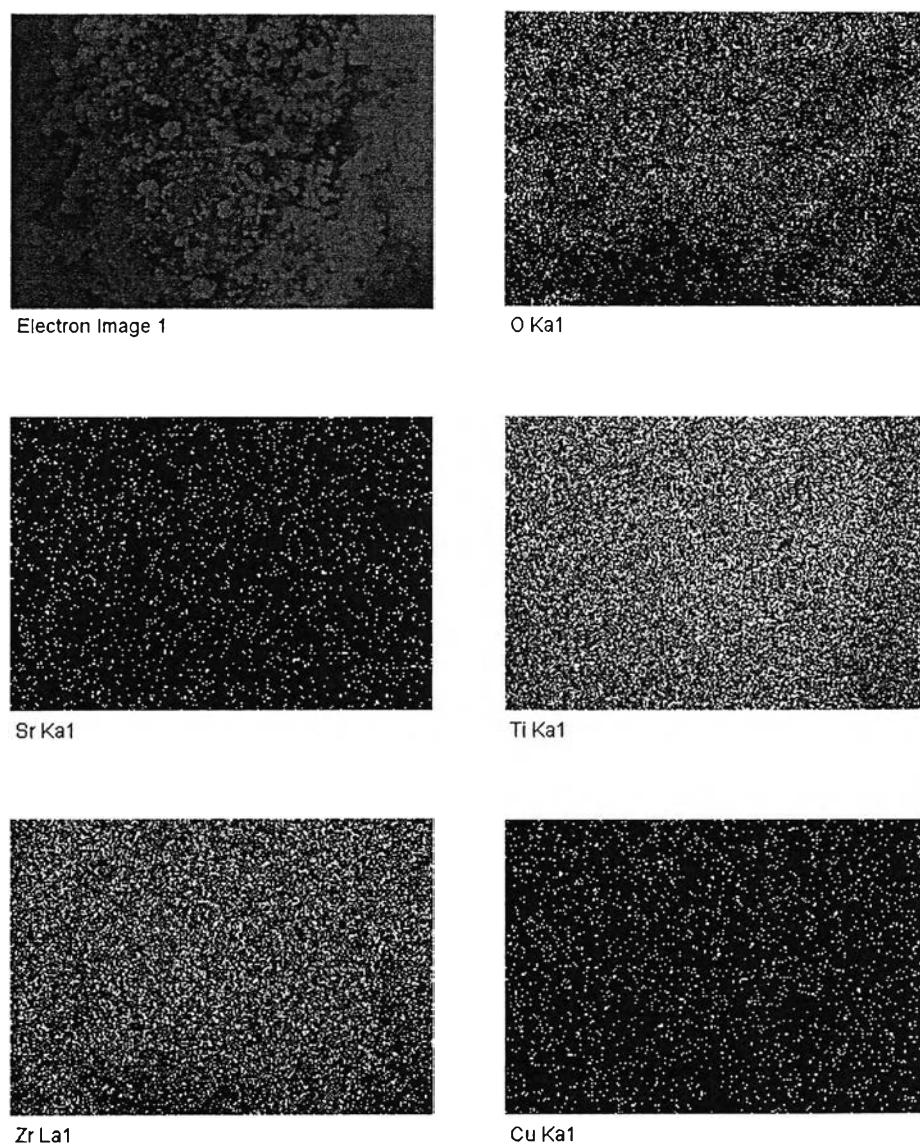
Figure 4.11 SEM image and EDX area mappings of the synthesized 0.25 wt.% Cu-loaded mesoporous-assembled $SrTi_{0.93}Zr_{0.07}O_3$ photocatalyst calcined at 700 °C for 4 h.
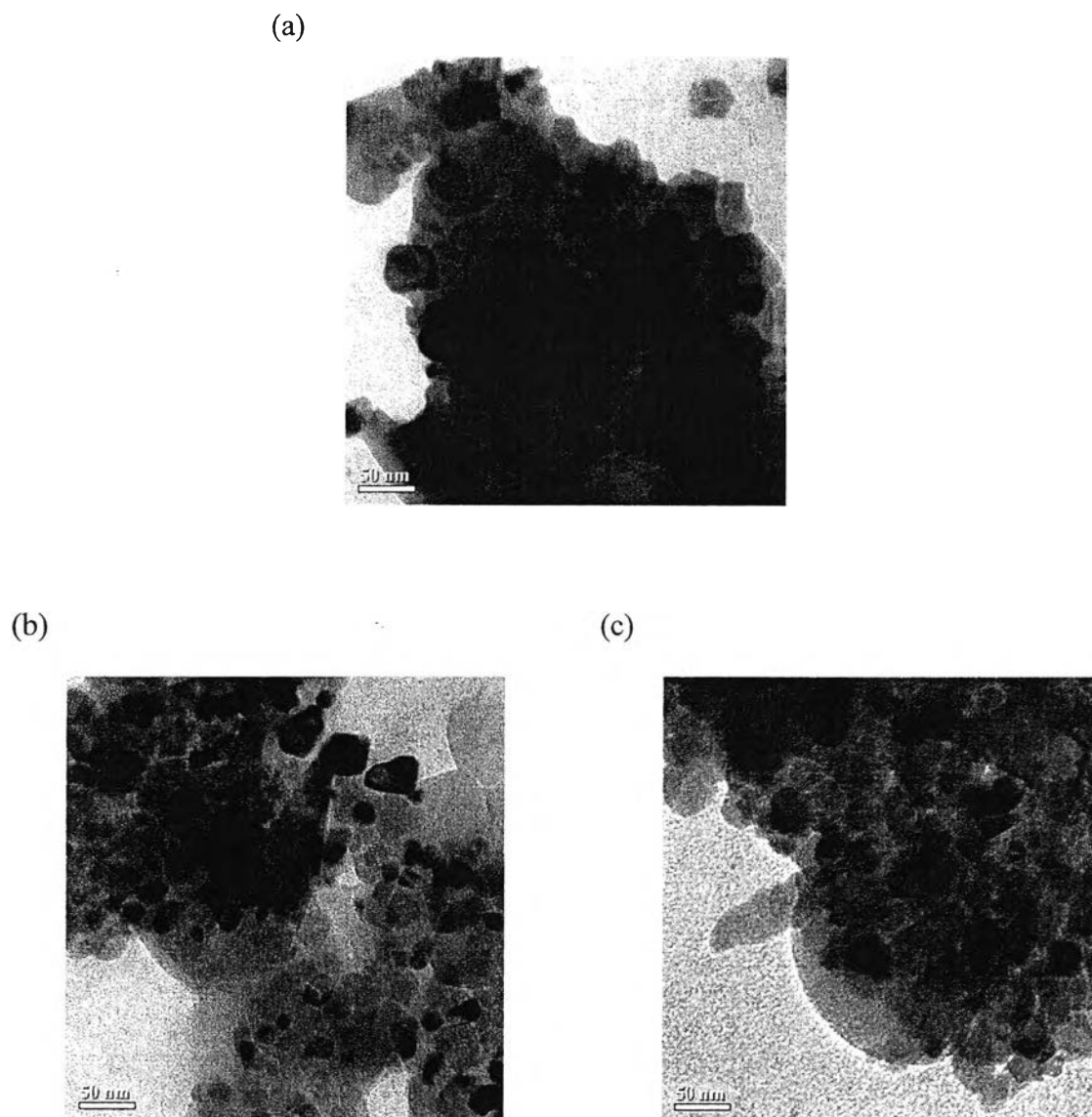
Electron Image 1

O Ka1

Sr Ka1

Ti Ka1

Si Ka1

Cu Ka1
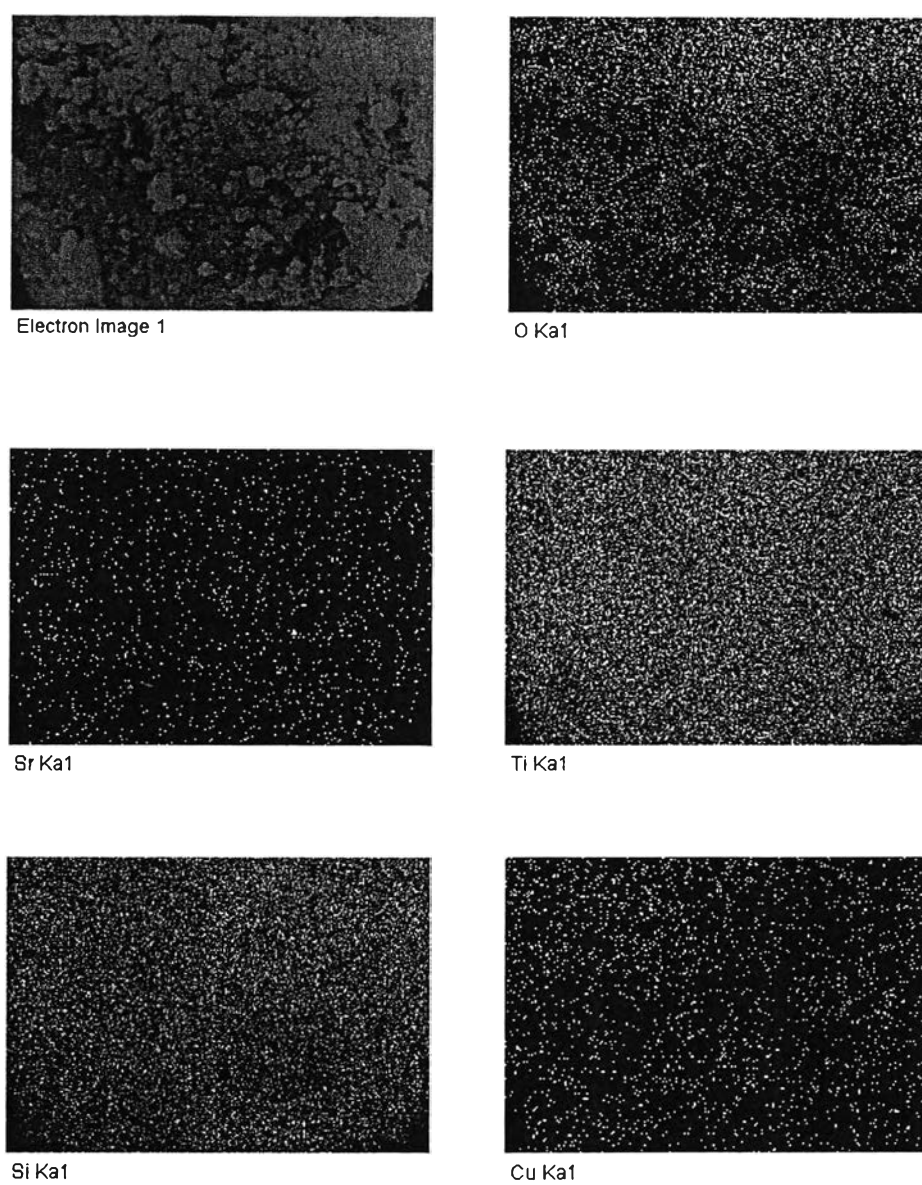
Figure 4.12 SEM image and EDX area mappings of the synthesized 0.75 wt.% Cu-loaded mesoporous-assembled $SrTi_{0.95}Si_{0.05}O_3$ photocatalyst calcined at 700 °C for 4 h.
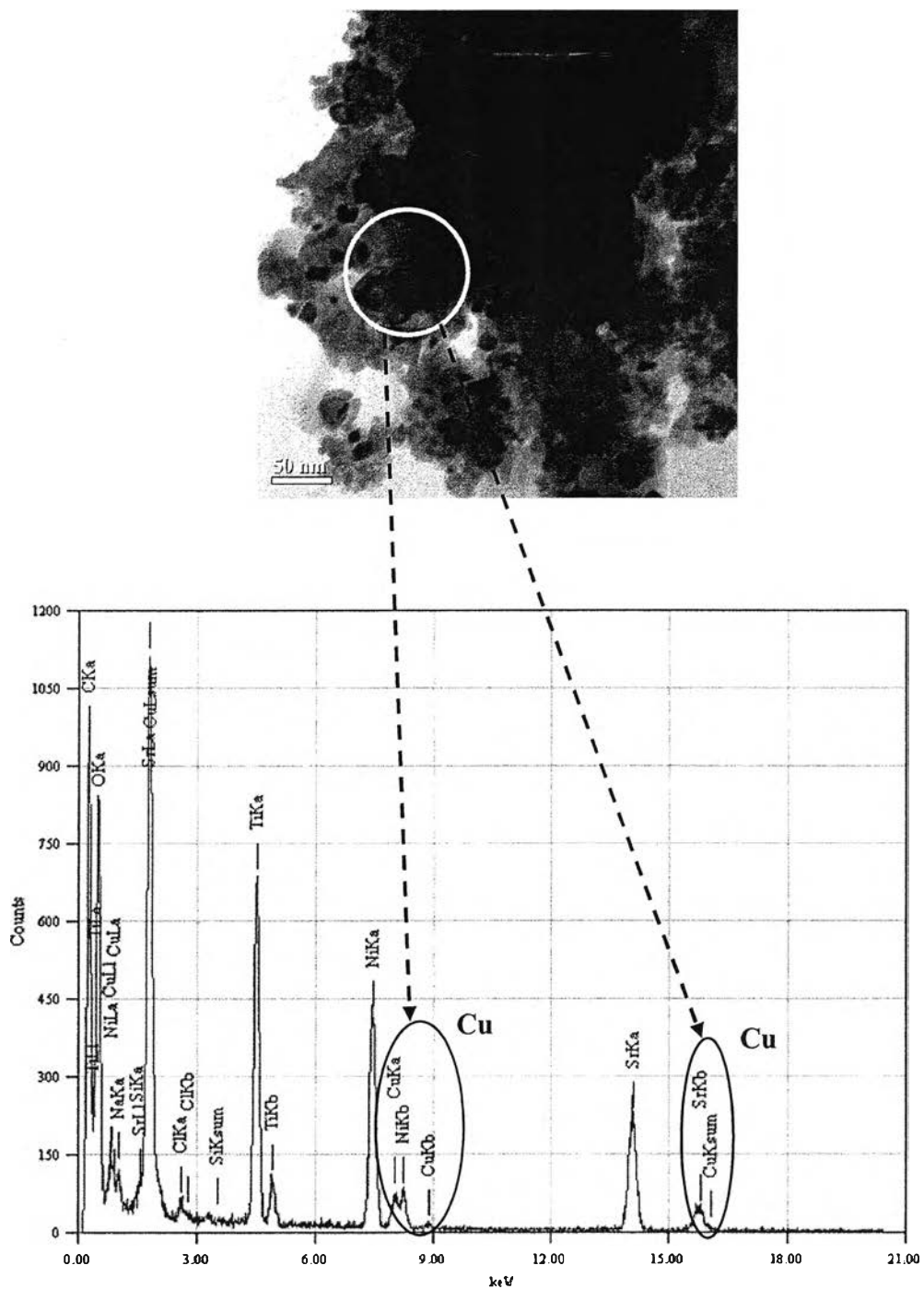
4.1.6 TEM-EDX Results

The TEM analysis was performed in order to obtain insight information about the particle sizes of the synthesized photocatalysts. The TEM images of the $SrTiO_3$, $SrTi_{0.93}Zr_{0.07}O_3$, and $SrTi_{0.95}Si_{0.05}O_3$ photocatalysts calcined at 700 °C are illustrated in Figure 4.13. The morphologies of the $SrTiO_3$, $SrTi_{0.9}Zr_{0.1}O_3$, and $SrTi_{0.95}Si_{0.05}O_3$ photocatalysts are the cubic shape, and their average particle sizes are in the range of 27-38, 20-27, and 27-32 nm, respectively. The observed particle sizes of the crystalline photocatalysts agree very well with the crystallite sizes calculated from the XRD patterns by the Scherrer equation, indicating a single crystalline characteristic. Besides, the TEM-EDX mapping analyses of the synthesized 0.25 wt.% Cu-loaded $SrTi_{0.93}Zr_{0.07}O_3$, and 0.75 wt.% Cu-loaded $SrTi_{0.95}Si_{0.05}O_3$ photocatalysts calcined at 700 °C were performed. As shown in Figures 4.14 and 4.15, the existence of the Cu nanoparticles on the $SrTi_{0.93}Zr_{0.07}O_3$ and $SrTi_{0.95}Si_{0.05}O_3$ photocatalysts was clearly observed, as confirmed by the EDX results. The average particle size of the loaded Cu is in the range of 15-20 nm.

(a)

(b)

(c)

Figure 4.13 TEM images of the synthesized mesoporous-assembled photocatalysts calcined at 700 °C for 4 h: (a) $SrTiO_3$, (b) $SrTi_{0.93}Zr_{0.07}O_3$, and (c) $SrTi_{0.95}Si_{0.05}O_3$.

Figure 4.14 TEM image and EDX point mapping of the synthesized 0.25 wt.% Cu-loaded mesoporous-assembled $SrTi_{0.93}Zr_{0.07}O_3$ photocatalyst calcined at 700 °C for 4 h.

Figure 4.15 TEM image and EDX point mapping of the synthesized 0.75 wt.% Cu-loaded mesoporous-assembled $SrTi_{0.95}Si_{0.05}O_3$ photocatalyst calcined at 700 °C for 4 h.

4.1.7 Hydrogen Chemisorption Results

Hydrogen chemisorption analysis was used to determine the metal dispersion. The Cu dispersion results over the synthesized Cu-loaded mesoporous-assembled $SrTi_{0.93}Zr_{0.07}O_3$ and $SrTi_{0.95}Si_{0.05}O_3$ photocatalysts are given in Table 4.7. The results show that the 0.25 wt.% Cu loading on $SrTi_{0.93}Zr_{0.07}O_3$ and the 0.75 wt.% Cu loading on $SrTi_{0.95}Si_{0.05}O_3$ gave the highest Cu dispersion for each individual photocatalyst. Further increase in Cu loading higher than such values of those photocatalysts negatively affected the Cu dispersion, probably due to the Cu nanoparticle agglomeration at very high Cu loadings. The Cu dispersion results can be related to the photocatalytic hydrogen production activity of the 0.25 wt.% Cu-loaded $SrTi_{0.93}Zr_{0.07}O_3$ and 0.75wt.% Cu-loaded $SrTi_{0.95}Si_{0.05}O_3$ photocatalysts, as described in the next section.

Table 4.7 Cu dispersion results of the Cu-loaded mesoporous-assembled $SrTi_{0.93}Zr_{0.07}O_3$ and $SrTi_{0.95}Si_{0.05}O_3$ photocatalysts calcined at 700 °C

| Photocatalyst	Cu loading (wt.%)	Cu dispersion (%)
$SrTi_{0.93}Zr_{0.07}O_3$	0.25	34.72
	0.50	23.96
	0.75	29.54
	1.0	13.52
	1.25	10.97
$SrTi_{0.95}Si_{0.05}O_3$	0.25	17.46
	0.50	28.54
	0.75	41.15
	1.00	21.54
	1.25	19.38

4.2 Photocatalytic Hydrogen Production Activity

In this research, the photocatalytic activity of the synthesized mesoporous-assembled $SrTi_xZr_{1-x}O_3$ and $SrTi_xSi_{1-x}O_3$ photocatalysts with different Ti-to-Zr or Ti-to-Si molar ratios calcined at various temperatures was investigated for hydrogen production from aqueous solution of methanol (50 vol.%) under UV light irradiation.

4.2.1 Effect of Ti-to-Zr and Ti-to-Si Molar Ratio

In this photocatalytic reaction, a 0.2 g of each of the synthesized mesoporous-assembled $SrTi_xZr_{1-x}O_3$ and $SrTi_xSi_{1-x}O_3$ photocatalysts was suspended in 200 ml of 50 vol.% methanol aqueous solution (100 ml methanol and 100 ml distilled water) at room temperature. The results of specific hydrogen production rate of the $SrTi_xZr_{1-x}O_3$ photocatalysts with various Zr molar ratios calcined at 700 °C are shown in Figure 4.16. It can be clearly observed that the specific hydrogen production rate reached a maximum value when using the $SrTi_{0.93}Zr_{0.07}O_3$ photocatalyst. From the specific surface area analysis (Table 4.2), it was clearly seen that the Zr addition could lead to an increase in the specific surface area when compared with the host $SrTiO_3$. This is responsible for the enhancement of the photocatalytic activity. In case of the $SrTi_xSi_{1-x}O_3$ photocatalysts, a similar behavior of the photocatalytic enhancement to the $SrTi_xZr_{1-x}O_3$ photocatalysts was observed, as also shown in Figure 4.16, and the highest specific hydrogen production rate was obtained when using the $SrTi_{0.95}Si_{0.05}O_3$ photocatalyst. However, the specific hydrogen production rate considerably decreased either with further increasing the Zr molar ratio higher than 7 mol.% or with further increasing the Si molar ratio higher than 5 mol.%. This is possibly because the Zr-rich $SrTi_xZr_{1-x}O_3$ or the Si-rich $SrTi_xSi_{1-x}O_3$ photocatalysts had too wide band gap energies (Table 4.6). These results agree well with the work of Khunrattanaphon *et al.* (2011), which reported the difficulty in band gap photo-excitation by UV light of wide band gap photocatalysts. Therefore, the number of electrons available to reduce water molecules subsequently decreases, resulting in the observed decrease in the specific hydrogen production

rate. From the overall results, the mesoporous-assembled $SrTi_{0.93}Zr_{0.07}O_3$ and $SrTi_{0.95}Si_{0.05}O_3$ photocatalysts were used for further experiments.
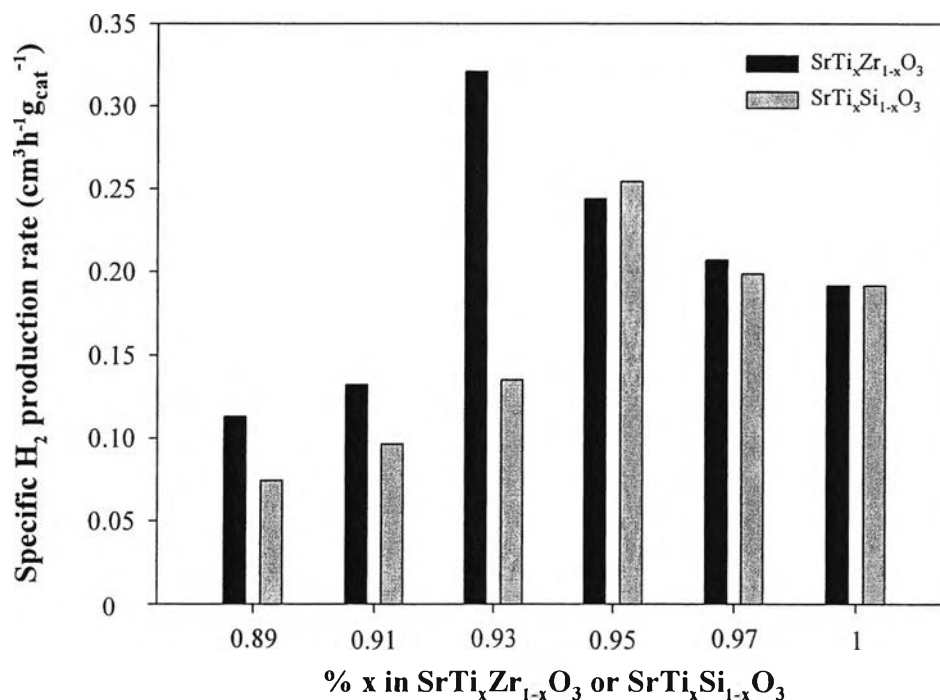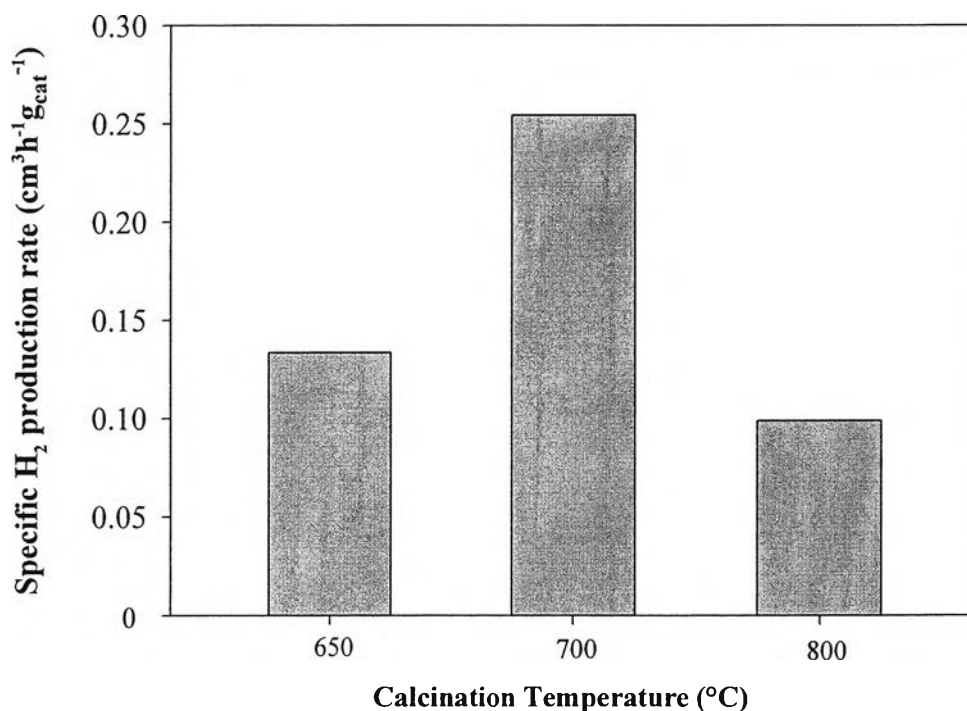

Figure 4.16 Effect of Ti-to-Zr and Ti-to-Si molar ratios on specific hydrogen production rate over the synthesized mesoporous-assembled $SrTi_xZr_{1-x}O_3$ and $SrTi_xSi_{1-x}O_3$ photocatalysts calcined at 700 °C (Photocatalyst, 0.2 g; total volume, 200 ml containing distilled water 100 ml and methanol 100 ml; and UV irradiation time, 5 h).

4.2.2 Effect of Calcination Temperature

Calcination temperature has a significant effect on the physicochemical properties and crystalline structure of a photocatalyst that definitely lead to the change in photocatalytic hydrogen production activity. The results of photocatalytic hydrogen production activity of the $SrTi_{0.95}Si_{0.05}O_3$ photocatalyst calcined at various temperatures in the range of 650 °C to 800 °C are shown in Figure 4.17. It is clearly seen that the maximum specific hydrogen production rate of $SrTi_{0.95}Si_{0.05}O_3$ photocatalyst of 0.25 $cm^3h^{-1}g_{cat}^{-1}$ was observed at 700 °C. The lower photocatalytic activity with the increase in calcination temperature is mainly because

of a large decrease in the specific surface area (Table 4.2). In addition, a significant increase in the crystallite size was observed when increasing calcination temperature (Table 4.4), resulting in a higher probability of charge carrier recombinations at the bulk traps. This suggests that a good control of crystallite size is required in order to prevent any charge carrier recombinations.

Figure 4.17 Effect of calcination temperature on specific hydrogen production rate over the synthesized mesoporous-assembled $SrTi_{0.95}Si_{0.05}O_3$ photocatalysts (Photocatalyst, 0.2 g; total volume, 200 ml containing distilled water 100 ml and methanol 100 ml; and UV irradiation time, 5 h).
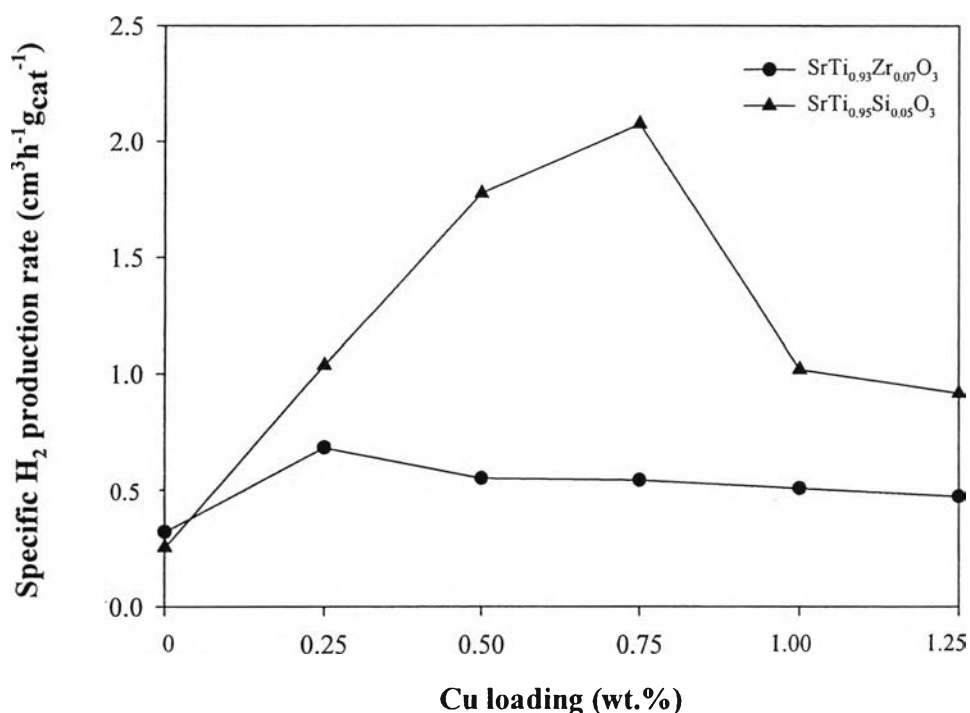
4.2.3 Effect of Cu Loadings

The hydrogen production activity of the Cu-loaded mesoporous-assembled $SrTi_{0.93}Zr_{0.07}O_3$ and $SrTi_{0.95}Si_{0.05}O_3$ photocatalysts calcined at 700 °C with various Cu loadings prepared by the PCD method was further investigated. Figure 4.18 represents their specific hydrogen production rate as a function of Cu loading. In overall, it can be clearly seen that the Cu loading had a positive effect on the enhancement of the photocatalytic hydrogen production activity of both the

mesoporous-assembled $SrTi_{0.93}Zr_{0.07}O_3$ and $SrTi_{0.95}Si_{0.05}O_3$ photocatalysts. This is possibly because the loaded Cu nanoparticles can induce the Schottky barrier with the mesoporous-assembled $SrTi_{0.93}Zr_{0.07}O_3$ and $SrTi_{0.95}Si_{0.05}O_3$ photocatalysts, which helps expedite the electron capture at the surface Cu active sites to further induce the photocatalytic hydrogen production (Puangpetch, et al., 2010). For the Cu-loaded $SrTi_{0.93}Zr_{0.07}O_3$ photocatalysts, the highest hydrogen production rate was obtained at 0.25 wt.% Cu loading, and a decrease in the specific hydrogen production rate with further increasing Cu loading to 1.25 wt.% was observed. In the same manner, the specific hydrogen production rate of the Cu-loaded $SrTi_{0.95}Si_{0.05}O_3$ photocatalysts increased with increasing Cu loading, reached a maximum value at the Cu loading of 0.75 wt.% before decreasing when the Cu loading was higher than 0.75 wt. %. Thus, these results indicate that the Cu loadings of 0.25 wt.% and 0.75 wt.% were the most suitable Cu contents for the synthesized mesoporous-assembled $SrTi_{0.93}Zr_{0.07}O_3$ and $SrTi_{0.95}Si_{0.05}O_3$ photocatalysts, respectively. Because the loading of Cu nanoparticles significantly increased the specific surface area of the host mesoporous-assembled $SrTi_{0.93}Zr_{0.07}O_3$ and $SrTi_{0.95}Si_{0.05}O_3$ photocatalysts while their crystallite sizes remained almost unchanged with varying Cu loading, as shown in Tables 4.5, the increase in the specific hydrogen production rate with increasing Cu loading from 0 wt.% to 0.25 wt.% for the $SrTi_{0.93}Zr_{0.07}O_3$ photocatalyst and from 0 wt.% to 0.75 wt.% for the $SrTi_{0.95}Si_{0.05}O_3$ photocatalyst can be mainly explained by the increase in Cu dispersion in the investigated Cu loading range (Table 4.7). The maximum Cu dispersions of the 0.25 wt.% Cu-loaded $SrTi_{0.93}Zr_{0.07}O_3$ and 0.75 wt.% Cu-loaded $SrTi_{0.95}Si_{0.05}O_3$ photocatalysts could plausibly enhance the photocatalytic reaction by promoting the most efficient charge carrier separation and serving as the active hydrogen production sites. When the Cu loading exceeded such critical limits (i.e. the optimum Cu loadings of 0.25 wt.% and 0.75 wt.% for the $SrTi_{0.93}Zr_{0.07}O_3$ and $SrTi_{0.95}Si_{0.05}O_3$ photocatalysts, respectively), the agglomeration Cu nanoparticles may take place, which was verified by the decreased Cu dispersion. The agglomerated Cu nanoparticles with high population at high Cu loadings can unavoidably act as the charge recombination centers, negatively resulting in a decrease in the photocatalytic hydrogen production activity (Zou et al., 2007). At the optimum Cu loadings of 0.25 wt.% and 0.75 wt.% for the $SrTi_{0.93}Zr_{0.07}O_3$ and

$SrTi_{0.95}Si_{0.05}O_3$ photocatalysts, the specific hydrogen production rates of 0.68 $cm^3/h\cdot g_{cat}$ and 2.08 $cm^3/h\cdot g_{cat}$ were observed, respectively. As compared to the unloaded $SrTi_{0.93}Zr_{0.07}O_3$ and $SrTi_{0.95}Si_{0.05}O_3$ photocatalysts, the specific hydrogen production rates were significantly enhanced by 112.5% and 717.3% at the optimum Cu loadings of 0.25 wt.% and 0.75 wt.%, respectively. Moreover, the 0.75 wt.% Cu-loaded $SrTi_{0.95}Si_{0.05}O_3$ photocatalyst calcined at 700 °C provided the highest hydrogen production activity, which was much higher than the 0.25 wt.% Cu-loaded $SrTi_{0.93}Zr_{0.07}O_3$ photocatalyst. This is possibly because the 0.75 wt.% Cu-loaded $SrTi_{0.95}Si_{0.05}O_3$ photocatalyst has a higher specific surface area (Table 4.3) and a higher UV light absorption ability (Figure 4.9).

Figure 4.18 Effect of Cu loading on specific hydrogen production rate over the synthesized mesoporous-assembled $SrTi_{0.93}Zr_{0.07}O_3$ and $SrTi_{0.95}Si_{0.05}O_3$ photocatalysts (Photocatalyst, 0.2 g; total volume, 200 ml containing distilled water 100 ml and methanol 100 ml; and UV irradiation time, 5 h).